J. Electrochem. Sci. Eng. **15(2)** (2025) 2451; http://dx.doi.org/10.5599/jese.2451

Open Access : : ISSN 1847-9286
https://pub.iapchem.org/ojs/index.php/JESE

Original scientific paper

High-performance supercapattery with nanotube-TiO_2/carbon nano tubes anode and coconut-shell-derived activated carbon cathode

Thi Thu Trang Nguyen[1,✉], Thi Nhu Nguyet Pham[2,3], Hoang Anh Nguyen[2,3], Thi Nhu Quynh Nguyen[2,3], Nguyen Thanh Le Huynh[2,3,✉], Van Viet Pham[4], Hoang Nguyen[2,3], Viet Hai Le[2,3], Thi Thu Trang Nguyen[5], Thi Thom Nguyen[1], Thi Nam Pham[1], Dai Lam Tran[1,6], Trong Lu Le[1]

[1]*Institute for Tropical Technology, Vietnam Academy of Science and Technology, Hanoi, Vietnam*
[2]*Vietnam National University Ho Chi Minh City, Vietnam*
[3]*University of Science, Ho Chi Minh City, Vietnam*
[4]*HUTECH University, Ho Chi Minh City, Vietnam*
[5]*University of Education, Ho Chi Minh City, Vietnam*
[6]*Graduate University of Science and Technology, Vietnam Academy of Science and Technology, Hanoi, Vietnam*

Corresponding authors: ✉*ntttrang@itt.vast.edu*; ✉*hltnguyen@hcmus.edu.vn*

Received: August 5, 2024; Accepted: December 23, 2024; Published: February 23, 2025

Abstract

This paper aims to present the fabrication of a Li-ion supercapattery by an anode designed for a lithium-ion battery (nanotube TiO_2 (NT-TiO_2) and carbon nanotubes (CNTs), namely as NT-TiO_2/CNTs) with a cathode designed for an electrochemical double-layer capacitor (derived activated carbon), resulting in high energy and densities of power. The hydro-thermal route formed the composite NT-TiO_2/CNTs. DFT calculations provide the Li absorbed inside and outside isolated CNTs and NT-TiO_2/CNTs. The lithium diffusion energy barrier results show that Li is preferred energetically inside CNT. The energy barrier of Li diffusion for isolated CNTs is 1.21 eV, whereas that of NT-TiO_2/CNTs is computed at 0.69 eV. It demonstrated that the functionalized NT-TiO_2 improves the performance and the rate of Li diffusion of the isolated CNTs system, which agrees with the experiment. The results illustrate that the synergistic effect of high conductive CNT networks and well-dispersed NT-TiO_2 structure can enhance hybrid capacitors' power and energy density through the brief diffusion routes for Li-ions and rapid transference of electrons. A Li-ion supercapattery battery, NT-TiO_2/CNTs-1||activated carbon (AC), achieved an energy density of 48.9 Wh kg^{-1}, surpassing supercapacitors, and a power density of 1667 W kg^{-1} at a current rate of 1 A g^{-1}, exceeding that of Li-ion batteries.

Keywords
TiO_2/carbon nanotubes composite; hybrid Li-ion capacitor; density functional theory calculations; energy density; power density

Introduction

Storing energy by utilizing Li-ion batteries (LIBs) or supercapacitors does not yet meet hybrid and all-electric vehicles power and energy demands, primarily due to Faradaic reactions from the intercalation of Li-ions into the electrodes, LIBs can deliver a high energy density of approximately 150 Wh kg^{-1} [1-3]. Nonetheless, such energy storage systems have limitations, including short cycling lifetimes and low power densities caused by the resulting volumetric strain and inherently sluggish diffusion of solid-state lithium in bulk. Meanwhile, electrochemical double layer capacitors (EDLCs) offer prolonged electrochemical stability (roughly 10,000 cycles) and high capacity of power (2 to 5 kW kg^{-1}); nevertheless, these systems have minimal energy density (3 to 6 Wh kg^{-1}) for EDLCs due to limited charge accumulation [4,5]. Therefore, the invention of a hybrid Li-ion capacitor (LIC) that merges the merits of both aforementioned technologies can be considered a potential candidate for a revolutionary energy storage system. Hybrid Li-ion capacitors, or supercapatteries, typically feature supercapacitor electrodes (made of carbonaceous materials forming electric double layers) on one side and Li-ion intercalating electrodes on the other [6,7]. With this setup, the device stores charge *via* reversible anion adsorption/desorption on the cathode surface and reversible lithium-ion insertion/extraction in the anode material [8].

Titanium dioxide (TiO_2) has drawn considerable attention as a battery electrode material. Due to its high chemical stability, affordability, abundant availability, and multiple oxidation states (III to V), it is applied in various fields, such as storing energy, photocatalysis, and dye degradation [5,9-11]. Nonetheless, a significant challenge for battery-type TiO_2 electrodes that limits their energy-storage performance is the insufficient cycling stability and electronic conductivity. This inadequacy, particularly during cycling, can lead to a loss of electrochemical sites [12]. Employing a $LiPF_6$-EC/DMC/DEC electrolyte with a concentration of 1 M, a cathode of carbon nanotube, and an anode of TiO_2-B nanowire, the hybrid Li-ion capacitor achieves a high energy density, which was 12.5 Wh kg^{-1} [13]. Other studies have also reported on LICs using the compound of titanium anode electrodes. While these devices show a slight increase in energy density, their power capability remains constrained by the slow intercalation electrode reaction in LICs. Research suggests that growing an ordered array architecture directly on conductive substrates can address the limitations of mixing with polymer binders or conductive carbon while providing efficient transport pathways for ions and electrons [7,14].

Activated carbon (AC) is used widely for the cathode electrode in a hybrid Li-ion capacitor because of its excellent contact area and electrical conductivity [15-17]. Nonetheless, this is attributed to the limited ion transport through small tunnels due to the restricted ion transportation, which reduces electrochemical surface accessibility. Thus, finding alternative carbon materials that offer better power density and energy in an organic electrolyte is crucial. A coconut-shell-derived AC is one of the popular biomass-derived ACs that has received enormous attention in the electrochemical capacitor industry [18,19]. The supercapattery based on nanotube-TiO_2/carbon nanotubes||activated carbon (NT-TiO_2/CNTs||AC) offers high energy density, fast charge-discharge cycles, and a long lifespan. These features make them ideal for key applications, such as stabilizing renewable energy systems (like solar and wind), enhancing energy efficiency in electric vehicles by capturing regenerative braking energy, and providing fast-charging solutions in portable electronics. Their ability to manage energy fluctuations makes them valuable in smart grid systems.

Herein, we have developed a hybrid Li-ion capacitor constructed with synthesized NT-TiO_2/CNTs and coconut-shell-derived AC. The hydrothermal structure is used to prepare the composites of the nanotube structure of TiO_2 and CNTs.

Experimental

Preparation of NT-TiO_2/CNTs nanocomposite

All chemicals were of high purity grade and were used without purifying. The NT-TiO_2/CNTs nanocomposites were prepared *via* a hydrothermal route. Initially, 1.13 g of TiO_2 was dispersed in 103.8 mL of NaOH with a concentration of 10 M and was magnetically stirred for one hour. After that, this mixture was transferred to a Teflon-lined autoclave before heating for 18 hours at 180 °C. This was followed by the step that the carbon nanotubes were added with distinct weight present, including 1, 3, and 5 wt.% of CNTs; the samples were marked as NT-TiO_2/CNTs-1, NT-TiO_2/CNTs-3, NT-TiO_2/CNTs-5, respectively. Next, 5 mL of deionized water was added to the solution, which was stirred for 1 hour until homogeneous. The resulting powder was then calcined at 500 °C for 2 hours at a heating rate of 5 °C min^{-1}. The residue was washed with deionized water and dried at 100 °C for 24 hours. For comparison, the same procedure was applied to prepare the pristine TiO_2 without CNTs, referred to as pristine NT-TiO_2.

Structural and morphological characterization of nanocomposite NT-TiO_2/CNTs

The nanocomposites NT-TiO_2/CNTs were analyzed using X-ray diffraction (XRD) on a D8 Advance diffractometer (Bruker) equipped with a LYNXEYE detector, with a Cu anode ($\lambda_{K\alpha}$ = 0.15689 nm) in the scan range of 20 to70° (0.02°/step). Raman scattering spectra were measured using an XPLORA spectrometer (HORIBA) with an excitation laser wavelength of 532 nm, and a measurement range from 50 to 2000 cm^{-1}. The pore volume distribution and specific surface area were determined by the Brunauer-Emmett-Teller (BET) method on a TriStar II-3000 (Micromeritics, USA). The morphology and particle size characteristics of composites were also examined by transmission electron microscopy (TEM) using a FEI Tecnai G2 F20 (USA).

Electrochemical characterization

The synthesized powders were combined in a porcelain mortar and pestle with acetylene black and polyvinylidene fluoride (PVDF) in a weight ratio of 80:15:5, respectively. The mixture was then coated onto the base (aluminum foil) to a 0.1 mm thickness, dried at 100 °C for 12 hours, and pressed to a final thickness of 200 µm; the mass density of the electrode was controlled around 10 mg cm^{-2}. The electrode preparation was detailed in the Supplementary material. The cell was assembled with the prepared anodes and lithium metal as the counter electrode. The electrolyte $LiPF_6$ 1 M in a 1:1 EC:DMC (v/v) was used at 150 µL, with three Whatman glass fibers as the separator. The full cell NT-TiO_2/CNTs-1||AC was assembled using coin-cell CR2032 type, the anode was the NT-TiO_2/CNTs composite electrode, and the cathode was the coconut-shell-derived AC electrode. The details of AC cathode preparation process are described in the Supplementary material. The LANHE CT2001A apparatus (China) was utilized at various current rates within a 0.o to 3.0 V voltage range to test the galvanostatic charge/discharge performance. The capacitance from GCD curves was calculated by Equation (1). The Ragone plot is constructed by plotting specific energy, E / Wh kg^{-1}, against specific power, P / W kg^{-1}, using the data from GCD curves, Equations (2) and (3):

$$C_{sp} = \frac{I\Delta t}{mV} \quad (1)$$

$$E = \frac{1}{2\times 3.6} C_{sp} V^2 \quad (2)$$

$$P = \frac{3600E}{\Delta t} \quad (3)$$

where C_{sp} / F g^{-1} is the specific (gravimetric) capacitance of the cell, I / A is the applied current, Δt /s is the discharge time, m / g is the mass of both electrodes, V / V is the potential window, and the given numerical factors are time/mass conversion factors.

Computational details

This research used calculations based on the first principles of density functional theory (DFT) from the Vienna *ab Initio* Simulation Package (VASP) [20,21]. Core regions were treated using the projector augmented wave (PAW) pseudopotentials [22,23]. The combination of generalized gradient approximation (GGA) [24,25] and the Perdew-Burke-Ernzerhof (PBE) [26,27] scheme was used to describe the exchange and correlation potentials. The GGA-PBE function has been reported with well-reasonably described carbon-based systems [28-37]. In all calculations, Grimme's DFT-D3 was employed to describe van der Waals interactions between carbon atoms [38], with an energy cutoff of 600 eV. All atomic positions were optimized using the conjugate gradient method, with self-consistent field (SCF) force values and conversion energy set to 10^{-6} eV and 0.002 eV nm^{-1}, respectively. DFT calculations were conducted with a Monkhorst−Pack [39]. 2×2×1 k-point with the involvement of the DFT+U approach [40] because of the 3d electrons of Ti. Hubbard parameters with J set to 0.5 eV and U set to 6.0 eV were used to treat these electrons [41,42] along with Grimme's D3 dispersion corrections to account for van der Waals interactions [43]. The lithium diffusion paths were employed, utilizing the nudged elastic band (NEB) method [44] within six transition images.

Results and discussion

Structure and morphology of NT-TiO_2/CNTs

Figure 1a illustrates the XRD patterns of the pristine NT-TiO_2 and the composite NT-TiO_2/CNTs samples. All peaks align well with the anatase phase (JCPDF-01-078-2486), exhibiting tetragonal symmetry with the point space group I41/amd [45,46]. The CNT content does not significantly change the anatase structure. The central peak (101) is observed at 25.3°, showing significant dependence on the synthesis. Under the assumption that the Debye-Scherrer equation is valid for spherical particles, the crystallite size was calculated using Equation (4):

$$D = \frac{K\lambda}{\beta \cos\theta} \quad (4)$$

where D is the average crystallite size (nm), β the full width at half maximum (FWHM), θ the Bragg diffraction angle, K is the Scherer constant number (0.89), and λ the wavelength of X-ray (0.154 nm). The lattice parameters and average crystallite size are presented in Table 1.

Table 1. *Lattice parameters and average crystallite size of pristine NT-TiO_2 and NT-TiO_2/CNTs composites*

	$a = b$ / nm	c / nm	V / nm^3	D / nm
NT-TiO_2	0.37889	0.95537	0.13715	19.05
NT-TiO_2/CNTs-1	0.37879	0.95209	0.13661	14.57
NT-TiO_2/CNTs-3	0.37957	0.95552	0.13766	22.18
NTTiO_2/CNTs-5	0.37889	0.95537	0.13715	19.05

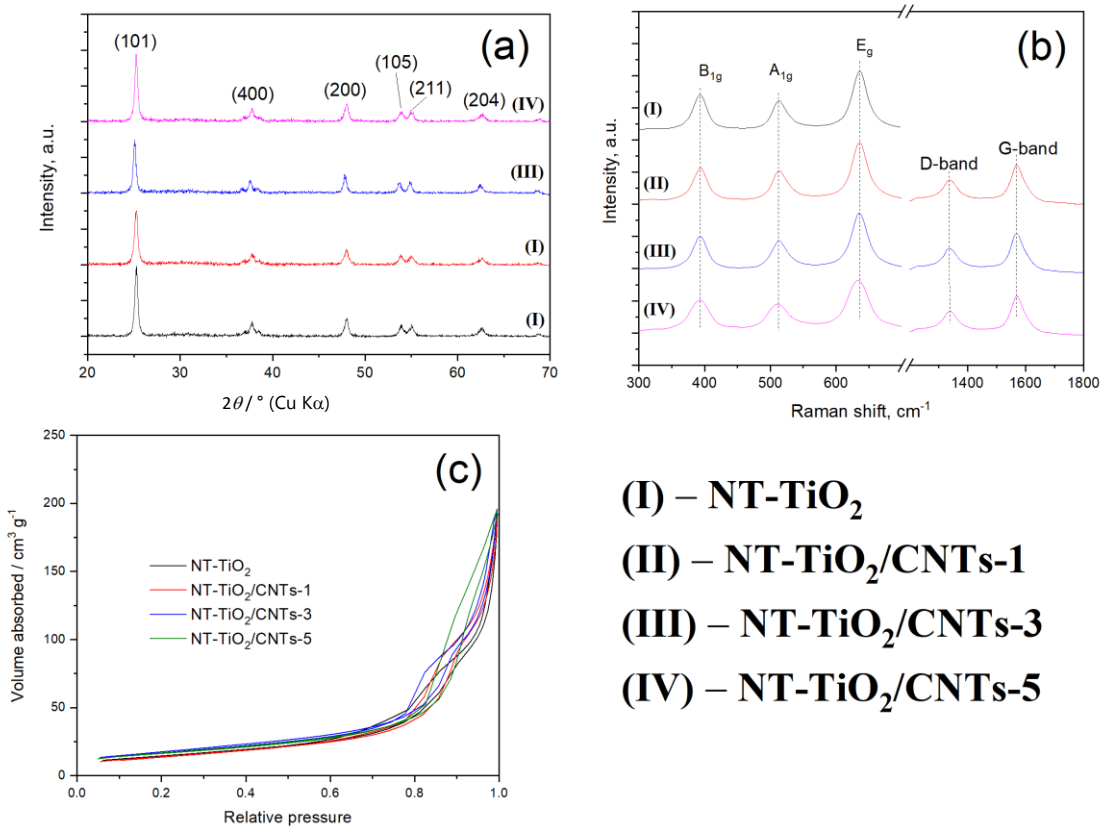

Figure 1. *(a) XRD diagrams, (b) Raman spectra and (c) nitrogen adsorption/desorption isotherm of pristine NT-TiO_2 and NT-TiO_2/CNTs composites*

Raman spectra (Figure 1b) show three features of the anatase phase NT-TiO_2 and the D-/G-bands of carbon. The characteristic bands in the low-frequency region (200 to 800 cm^{-1}) at 400, 515, and 639 cm^{-1} correspond to the anatase phase's B1g, A1g + B1g, and Eg modes. The B1g mode at 400 cm^{-1} is associated with Ti–O stretching vibrations. All the samples exhibit the anatase phase, the three active modes of TiO_2, corresponding to 397 (A_{1g}) and 639 (E_g) cm^{-1} [47,48]. Moreover, Raman spectroscopy is extensively employed to analyze the electronic structure of carbon-based materials. In the high-frequency region, the carbon Raman spectrum exhibits two distinct peaks: the D-band (1320 cm^{-1}) and the G-band (1571 cm^{-1}) [49,50].

Figure 1c compares the nitrogen adsorption/desorption isotherms at 77 K and the distribution in size. The multipoint BET method, based on adsorption data within the relative pressure (P/P_o) range of 0.05 to 0.30, was utilized to calculate the specific surface area, whereas the Barrett-Joyner-Halenda (BJH) desorption analysis was used to obtain the pore volume and average pore diameter. As a result, the isotherms display type IV behavior, characteristic of mesoporous materials, with hysteresis loops resembling type H3, indicating plate-like particle aggregates with slit-shaped pores. CNT loading notably affects the porous volume, with the maximum volume observed at a 0.05 ratio reaching approximately 162 m^2 g^{-1}, higher than the sample without CNTs. Although the BET surface area remains relatively unaffected by CNT loading, the BJH desorption analysis shows a correlation between porous volume and pore diameter. Pore sizes initially measured at 8.3 nm increase to 8.7 to 9.8 nm with CNT addition. The active surface area and average pore size are provided in Table 1.

Figure 2 illustrates TEM micrographs of NT-TiO_2/CNTs composites, revealing the interconnection of nanotubes. The morphology of NT-TiO_2 (Figure 2a) and NT-TiO_2/CNTs composites (Figure 2b to 2d) is uniform. The size of the nanotube is around 4-5 nm for the inner diameter and around 13-15 nm for

the outer diameter. The length of NT-TiO_2 can be found in the range of 100 to 150 nm. Moreover, fiber with a small diameter can be attributed to the CNT fiber. With a matrix interconnection, the NT-TiO_2/CNTs can promote electron transfer and Li-transportation in the electrochemical performance.

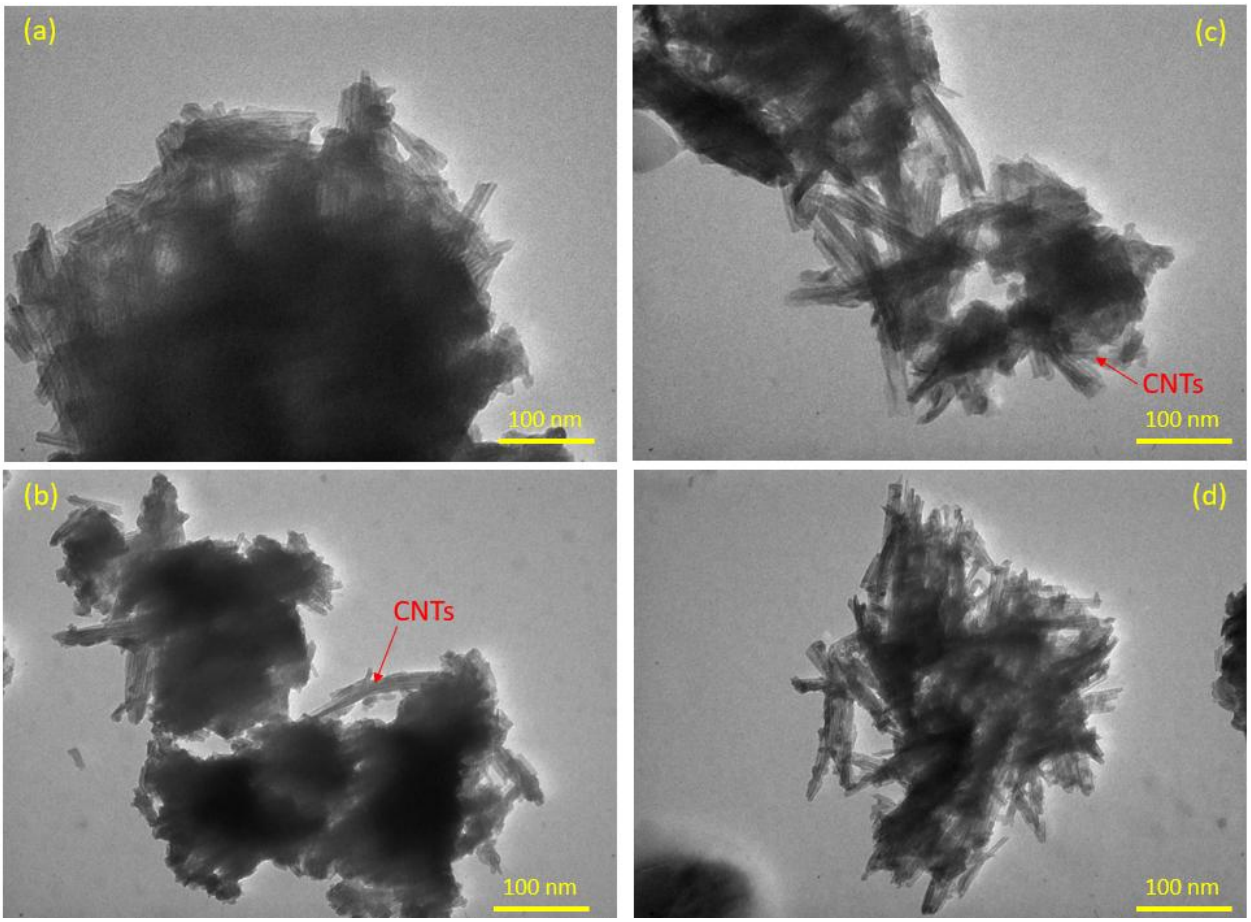

Figure 2. *TEM images of (a) pristine NT-TiO_2; (b) NT-TiO_2/CNTs-1; (c) NT-TiO_2/CNTs-3; (d) NT-TiO_2/CNTs-5 composites*

The survey XPS spectrum (Figure 3) reveals the presence of carbon, oxygen, and titanium, which validates the successful synthesis of the composite. In the high-resolution C1s spectrum, multiple carbon states are observed. The peak at 283.4 eV corresponds to sp^2 hybridized carbon, confirming the presence of intact carbon nanotubes. The C–O bonds at 284.8 eV may arise from functional groups on the CNTs or contaminants. Notably, the Ti–O–C interaction peak at 287.1 eV implies a robust interface between NT-TiO_2 and CNTs, which can enhance charge transfer in applications such as photocatalysis or energy storage. The O 1s spectrum exhibits two oxygen environments. The lattice oxygen in TiO_2 is shown at 528.4 eV, whereas the higher energy peak at 529.7 eV indicates surface-adsorbed oxygen species. The Ti 2p spectrum displays the expected spin-orbit splitting for Ti $2p_{3/2}$ and $2p_{1/2}$, confirming the presence of Ti^{4+} ions in the NT-TiO_2 crystal structure. The absence of lower binding energy peaks suggests that Ti is primarily in the +4-oxidation state without significant reduction to Ti^{3+}, which is favorable for maintaining the material's electronic properties. These XPS results confirm the successful fabrication of the NT-TiO_2/CNTs composite with a robust interfacial interaction. For supercapattery, the NT-TiO_2/CNTs interface could facilitate rapid electron transfer, improving charge/discharge rates and overall performance.

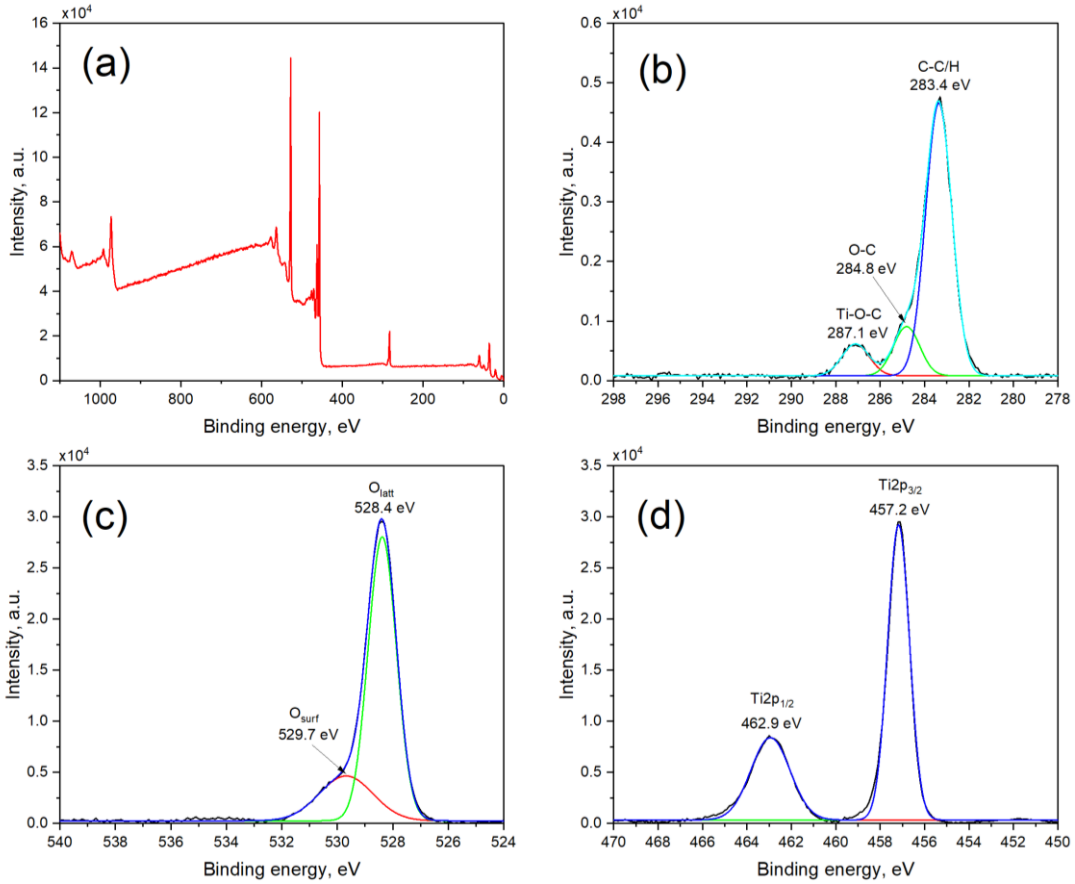

Figure 3. *XPS spectrum of NT-TiO_2/CNTs-1: (a) full-scan profile, and narrow profiles (b) carbon, (c) oxygen, and (d) titanium*

Electrochemical performance

Cyclic voltammetry (CV) studies were performed on the prepared samples within a voltage range of 1.5 to 2.5 V (*vs*. Li^+/Li) to investigate the lithiation and delithiation behavior. The CV curves of pristine NT-TiO_2 and NT-TiO_2/CNTs electrodes are shown in Figure 4a-d and carried out at many scan rates (from 0.01 to 0.4 mV s^{-1}). The cycles show a characteristic cathodic/anodic peak at 1.6 V and 2.0 V due to the insertion/de-insertion of Li^+ ions in the TiO_2 host. The area of CV curves indicates the total Li^+ storage capacity, which generally comprises two parts: (i) Faradaic contributions with the Li^+ diffusion-controlled redox reactions and (ii) non-Faradaic contributions from the double-layer capacitive effect. The cyclic voltammetry data were analyzed at different sweep rates using the following Equation (5):

$$I = av^b \quad (5)$$

The scan rate v influences the measured current I following a power law relationship, with a and b as adjustable parameters. The b-value is determined from the slope of the log I *versus* log v plot. A b-value of 1.0 indicates a capacitive surface process, whereas a b-value of 0.5 suggests a diffusion-controlled process corresponding to the Ti^{4+}/Ti^{3+} redox reaction. Figure 4e shows that plotting log I *versus* log v results in a linear relationship with slopes of b = 0.55 for the anodic process in NT-TiO_2 and b = 0.62 for the NT-TiO_2/CNTs-1 electrode. A b-value of 0.55 is close to 0.50, which suggests that charge storage within the scan rate range of 0.01 to 0.4 mV s^{-1} and a voltage window of 1.5 to 2.5 V is predominantly governed by diffusion-controlled insertion processes. Using Equation (6), the proportion of each contribution type is determined from the total charge storage at a given scan rate.

$$I = k_1 v + k_2 v^{1/2} \quad (6)$$

Equation (6) can be altered to the Equation (7):

$$I/v^{1/2} = k_1 v^{1/2} + k_2 \quad (7)$$

In Equation 6, the first term ($k_1 v$) represents the capacitive contribution to the current response, while the second term ($k_2 v^{1/2}$) reflects diffusion-controlled process contribution. The coefficients k_1 and k_2 are obtained from the linear fit as the slope and y-intercept of linear relation defined by Equation (7). The total current response is separated into individual contributions by utilizing these values, which are then used in Equation (6).

Figure S1 to Figure S4 in the Supplementary material exhibit the charge contributions determined from CV curves at different potential scan rates. By comparing the total area to the shaded area at a scan rate of 0.40 mV s^{-1}, the capacitive contributions are found to be 73.8, 78.2, 74.1 and 72.3 % of the total charge for the pristine NT-TiO_2 and NT-TiO_2/CNTs electrodes. A Ti^{4+}/Ti^{3+} redox reaction controls the diffusion-controlled charge at a given peak potential. Using the same approach, the contributions of the two charge storage processes at different scan rates are assessed and depicted in Figure 4f as a bar graph at a scan rate of 0.4 mV s^{-1}. With increasing scan rates, the capacitive contribution becomes the main factor determining the total charge stored in the cell. This increased capacitive effect at higher scan rates results from enhanced electron transfer due to a shorter Li^+ diffusion path, which supports rapid charge storage and better long-term cyclability. Moreover, the diffusion-controlled process at the electrode surface and throughout the electrode contributes to faster Li^+ kinetics, improved rate performance, and longer cycle life.

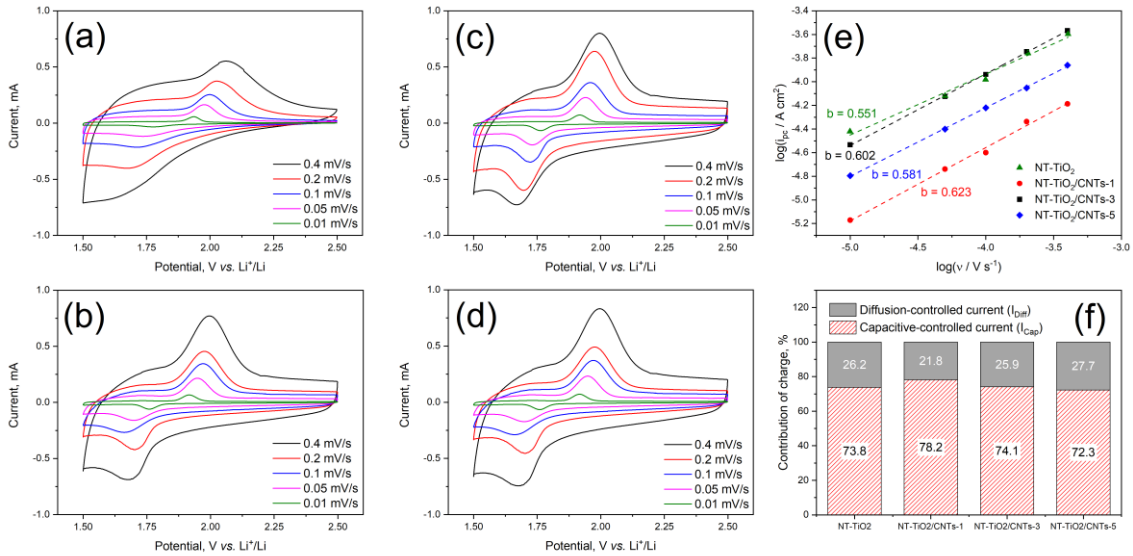

Figure 4. *Cyclic voltammetry curves of (a) pristine NT-TiO_2, (b) NT-TiO_2/CNTs-1, (c) NT-TiO_2/CNTs-3 and (d) NT-TiO_2/CNTs-5 electrodes at various sweep rates from 0.01 to 0.4 mV s^{-1}; (e) log* I vs. *log* v *and (f) charge contributions for electrodes at 0.4 mV s^{-1}*

The first charge-discharge curves at rate C/10 of NT-TiO_2 and NT-TiO_2/CNTs electrodes in 1.0 to 3.5 V in lithium half-cells are presented in Figure 5a-b, respectively. It has a notable reversible discharge capacity of 270 mAh g^{-1} and a Coulombic efficiency of 100 % for NT-TiO_2/CNTs-1 electrode. The capacities for other electrodes are found to be 207 mAh g^{-1} for pristine NT-TiO_2, 235 mAh g^{-1} for NT-TiO_2/CNTs-3 and 214 mAh g^{-1} for NT-TiO_2/CNTs-5. Long-term cycle performance is shown in Figure 5b. The NT-TiO_2/CNT-1 electrode delivers excellent cycle stability, maintaining 90 % capacity retention after 160 cycles. Moreover, the rate performance of the NT-TiO_2/CNTs-1 electrode is also measured

and presented in Figures 5c to 5d. It exhibits significantly outstanding rate capability, particularly at high C rates. It achieves capacities of 270, 235, 213, 193, 168, and 147 mAh g^{-1} at numerous current rates, including 0.1C, 0.2C, 0.5C, 1C, 2C, and 5C. These findings demonstrate that the NT-TiO_2/CNTs-1 electrode delivers a high reversible capacity, cycle stability, and outstanding rate performance.

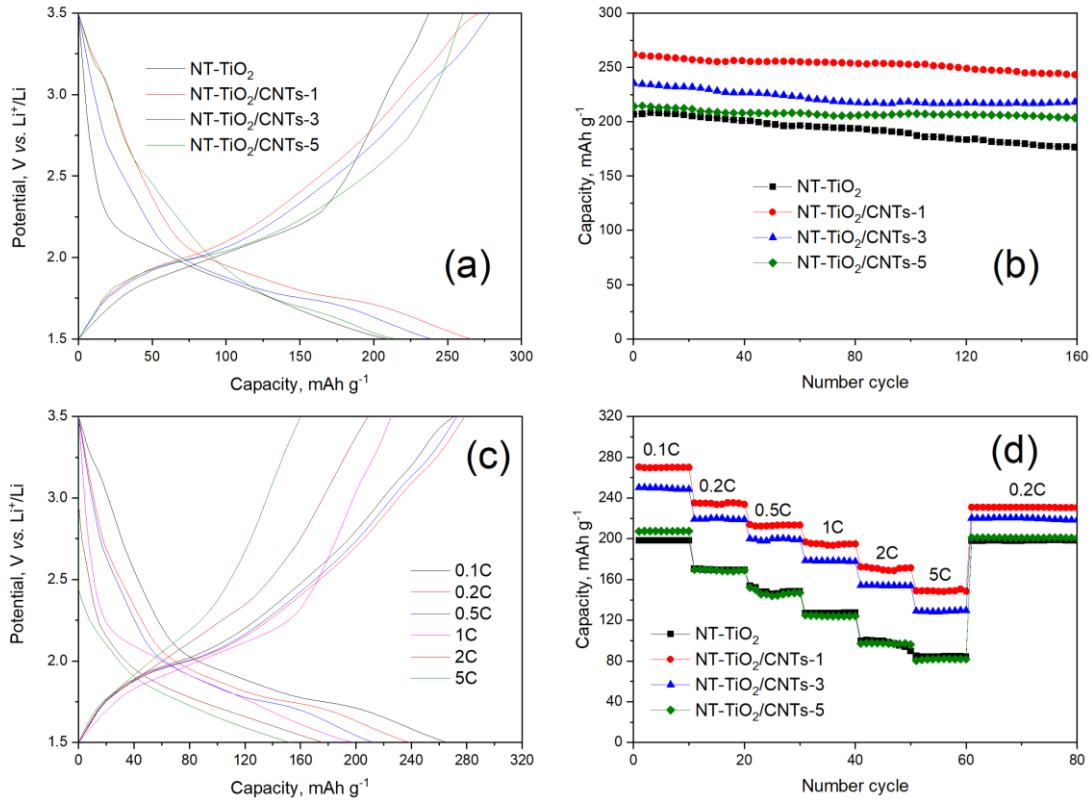

Figure 5. *(a) Charge/discharge curves and (b) cycling behavior of pristine NT-TiO_2 and NT-TiO_2/CNTs electrodes at rate 0.1C; (c) typical charge/discharge curves and (d) cycling behavior at various rates from 0.1C to 5C of pristine NT-TiO_2 and NT-TiO_2/CNTs electrodes*

Figure 6a displays the charge/discharge curves in the voltage window from 0-3 V of hybrid Li-ion capacitor in asymmetric configuration NT-TiO_2/CNTs||AC at different charge-discharge current rates and the long-term cycling stability at 10 A g^{-1} is shown in Figure 6c. As the current density discharge increases (0.2 to 10 A g^{-1}), the specific capacitances of the NT-TiO_2/CNTs||AC cells decrease because of the polarization effects and surface adsorption processes (Figure 6b). The specific capacitance is found to be 4.5 F g^{-1} for pristine NT-TiO_2||AC cell, 28.8 F g^{-1} for NT-TiO_2/CNTs-1||AC cell, 20.5 F g^{-1} for NT-TiO_2/CNTs-3||AC cell, and 15.1 F g^{-1} for NT-TiO_2/CNTs-5||AC cell at current rate 10 A g^{-1}. At high current densities, ions are near the surface of the electrode material due to the charge storage on the surface (non-Faraday mechanism), leading to a reduced capacitance value. The NT-TiO_2/CNTs-1||AC cell shows a suitable capacitance of 28.8 F g^{-1} at a current density of 10 A g^{-1}, and the capacitance retention is nearly 85 % upon 5000 cycles. Figure 6d illustrates the Ragone plot of asymmetric cells NT-TiO_2/CNTs||AC (AC: coconut-shell derived activated carbon). At the current density of 1 A g^{-1}, TiO_2/CNTs-1||AC asymmetry cell displays superior performance, exhibiting an energy density of 48.9 Wh kg^{-1} and a power density of 1677 W kg^{-1}. When the power density increases, the energy density of these electrodes decreases. Proportionally, NT-TiO_2/CNTs display a competitive performance compared with other hybrid supercapacitors [51-54].

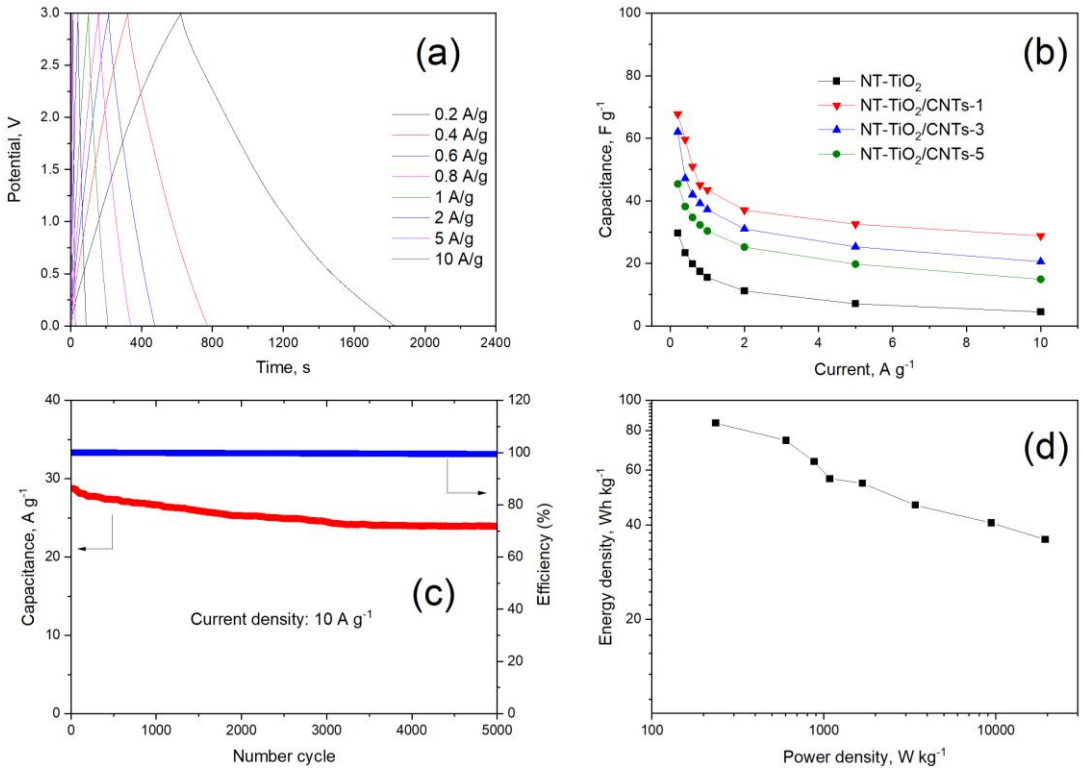

Figure 6. *(a) Charge/discharge curves of NT-TiO_2/CNTs-1||AC cells at various rates from 0.2 to 10 A g^{-1}; (b) specific capacitance vs. rate of NT-TiO_2/CNTs||AC cells; (c) cycling behavior of NT-TiO_2/CNTs-1||AC cell upon 5000 cycles at rate 10 A g^{-1} and (d) Ragone plot of NT-TiO_2/CNTs-1||AC*

Computational part

The equilibrium structures

The NT-TiO_2 was constructed via three layers of (101) anatase surface (55). The NT-TiO_2/CNTs system was built as the (101) TiO_2 anatase functionalized 4 ×4 armchair carbon nanotube (CNTs), as shown in Figure 7. The interlayer-connected distances between the top layer of TiO_2 and the surface of CNTs were most stable at 0.236 and 0.224 nm. The average C–C bond lengths of pristine CNTs and NT-TiO_2/CNTs were computed as 0.143 and 0.143 nm, respectively. These parameters are consistent with the previous study of CNTs25 and prove that our methodology is reasonable for further calculations.

The adsorption energies (E_{ads}) of lithium on pristine CNT and the system of TiO_2/CNT were computed as $E_{ads} = E_{Li+sys} - E_{Li} - E_{sys}$, where E_{Li+sys}, E_{Li} and E_{sys} are defined as the DFT-total energy of Li adsorbed on systems, the isolated Li atom at the most stable position, and the pristine CNT and TiO_2/CNT, respectively.

Table 2 reported that in both systems of CNT with and without the functionalized TiO_2, the value of Li adsorption energies suggests Li can adsorb at the inside and outside surface of CNT. The functionalization of nanotube TiO_2 improved the lithium adsorption behavior corresponding with the negatively higher Li adsorption energies than the system of isolated CNTs in interior and exterior Li adsorption. The higher negative value of the adsorption energy proves that the Li atom slightly prefers to adsorb at the exterior side of armchair CNTs, and the CNTs system with the functionalized TiO_2 agrees well with the precious study [56] and our experiment. These points are also consistent with the closer Li-CNTs distance with Li adsorbed inside and outside surface of CNT in NT-TiO_2/CNTs compared to an isolated CNTs system. The mobility of Li in the electrodes significantly influences the charge/discharge rate of the LIBs. The Li diffusion paths of CNTs and NT-TiO_2/CNTs were investigated through the NEB method, in which Li moves along different possible reaction paths.

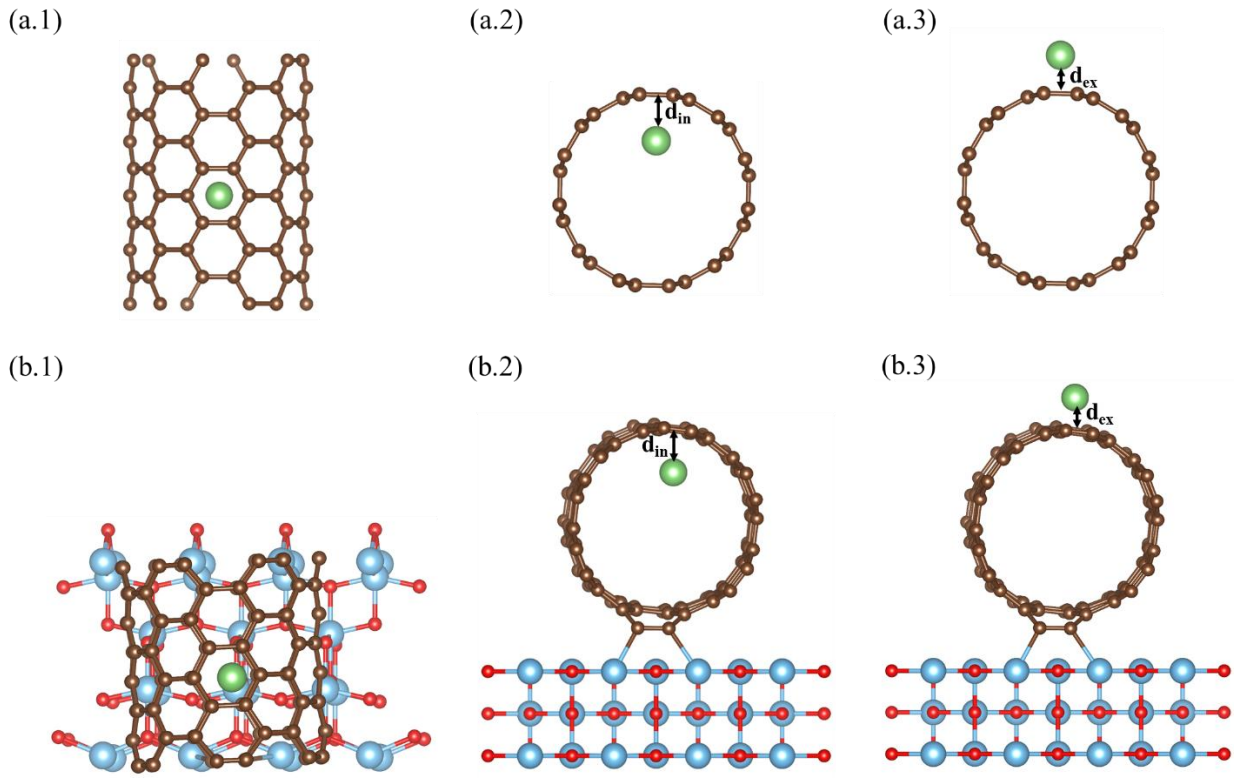

Figure 7. *The most stable configurations of (a.1) armchair 4 × 4 Carbon nanotube (CNTs) and (b.1) NT-TiO_2/CNT. They are absorbed by a lithium atom (green atom) and stable lithium interior (a.2) or exterior (a.3) of the CNTs. The adsorbed Li inside and outside NT-TiO_2/CNT were shown in (b.2) and (b.3), respectively. The brown, red, blue, and green spheres represent carbon (C), oxygen (O), titanium (Ti), and lithium (Li) atoms, respectively*

We studied the Li diffusion route by moving a lithium atom along the axis of the tube. The systems with Li atoms around the tube ends have much higher total energy than those on the inner or outer surface of the tube. This suggests that Li prefers to move across the CNTs wall and toward the direction of the open ends of CNT in both isolated 4×4 CNTs and NT-TiO_2/CNTs systems, as shown in Figure 8a-b. Figure 8c shows the energy diffusion barriers of isolated CNTs are 1.21 and 1.82 eV for the Li-interior and exterior surfaces of CNTs, respectively. In the case of NT-TiO_2/CNTs, the energy barrier of Li-CNTs interior is 0.69 eV, while lithium diffusing above the outer of CNTs should overcome a slightly higher energy barrier of 0.90 eV. The energy barrier for Li inside CNTs is lower than the CNTs out sites, matching well with the other theoretical study [57]. NT-TiO_2/CNTs in interior and exterior Li adsorption sites have lower energy barriers than the isolated system of CNTs. It demonstrated that the functionalization of NT-TiO_2 can enhance the performance and the rate of electron transfer of Li diffusion, which agrees with our experiment.

Table 2. Summary of the Li-CNTs distance in pristine CNTs and NT-TiO_2/CNTs system. d_{in} and d_{ex} are described for the distance between Li adsorbed position inside (Li-interior) and outside (Li-exterior) surface of CNTs and the centroid of the nearest corresponding hexagonal ring of CNTs, respectively

	Li-interior		Li-exterior	
	d_{in} / nm	E_{ads} / eV	d_{in} / nm	E_{ads} / eV
CNTs	0.0179	-1.42	0.0174	-1.67
NT-TiO_2/CNTs	0.0176	-1.66	0.0174	-1.74

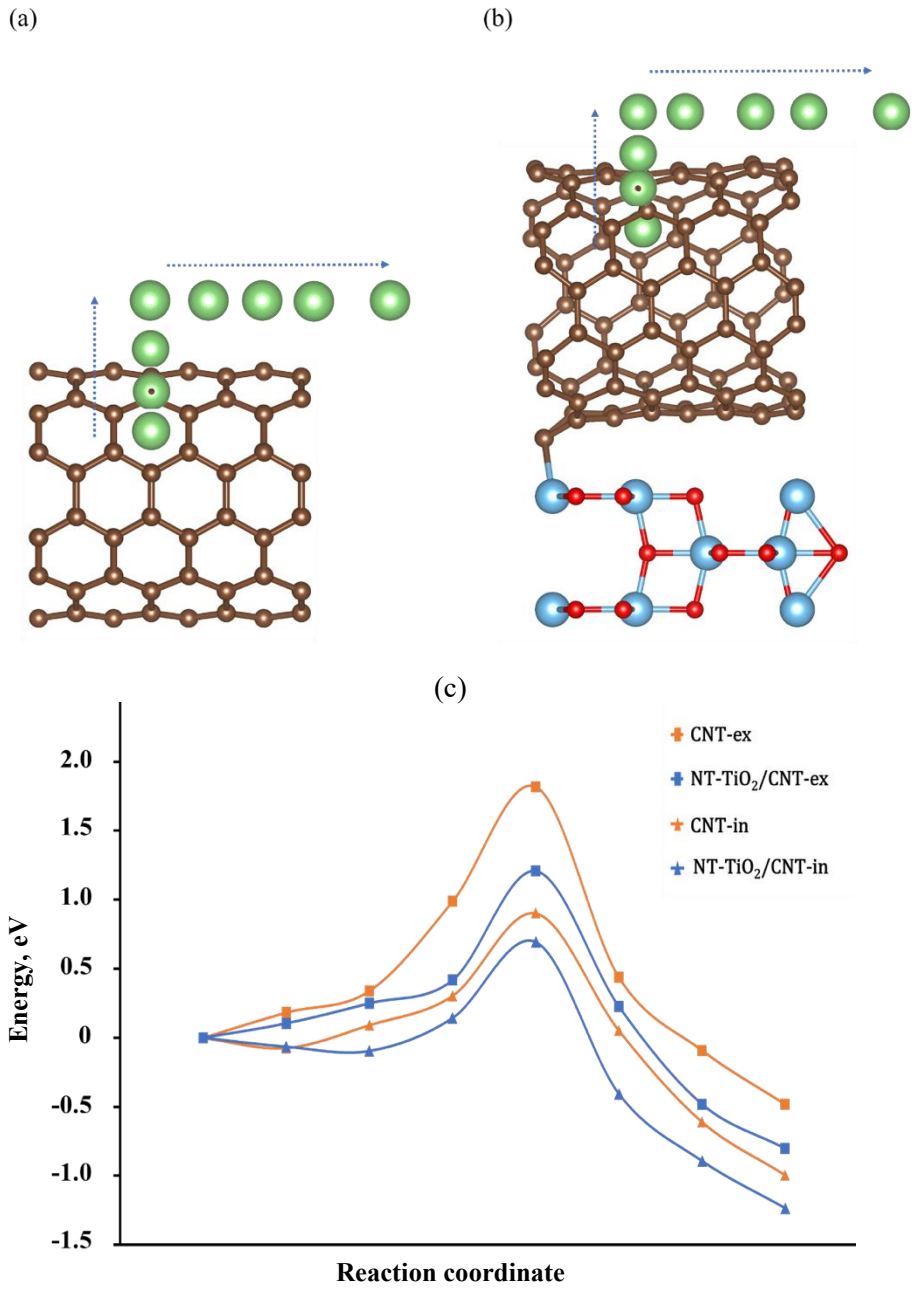

Figure 8. *The most stable diffusion paths of Li via 6 transition steps for (a) CNT, (b) NT-TiO_2/CNTs. (c) The profile energy barrier of Li diffusion for CNTs and NT-TiO_2/CNTs with the interior and exterior Li adsorption*

Conclusions

In conclusion, we have successfully designed the composites of nanotube structure TiO_2 with CNTs *via* a hydrothermal route. A high-performance supercapattery was developed and tested, featuring an NT-TiO_2/CNTs anode and a coconut-shell-derived AC cathode. The results indicate that the synergistic effect of well-dispersed NT-TiO_2 structure and high conductive CNTs network can improve hybrid capacitors' energy and power density through the short Li-ion diffusion paths and the quick electron transfer. The NT-TiO_2/CNTs-1||AC asymmetric cell displayed high energy density versus power density (48.9 *vs.* 1667 W kg^{-1}) at current rate 1 A g^{-1} and superior cycle stability at 10 A g^{-1} with capacitance retention of nearly 85 % after 5000 cycles. The DFT calculations provide two possible interior and exterior Li absorbed on CNTs and NT-TiO_2/CNTs. The energy diffusion barrier of Li at the inside and outside surfaces of isolated CNTs are computed at 1.21 and 1.82 eV, respectively. Besides that, the NT-TiO_2/CNTs also proved that the Li-interior diffusion energetically

is more favorable than that of Li-exterior, with a lower energy barrier of 0.21 eV. The Li diffusion energy barrier of Li located on the inside surface of isolated CNTs and NT-TiO_2/CNTs are 1.21 and 0.69 eV, respectively. Our experiment and theoretical results demonstrated that NT-TiO_2 is promising to enhance the electron transfer rate and Li diffusion of isolated CNTs.

Supplementary material: *Additional data are available electronically on article page of the journal's website: https://pub.iapchem.org/ojs/index.php/JESE/article/view/2451, or from the corresponding author upon request.*

Data availability: *The data supporting the findings of this study can be obtained from the corresponding author upon request.*

Declaration of competing Interest: *The authors have stated that they have no financial interests or personal connections that might have impacted the results presented in this paper.*

Acknowledgments: *This work was financially supported by the Vietnam Academy of Science and Technology (VAST) under the grant number VAST07.01/23-24.*

Tang T.T. Nguyen, Nguyet N.T. Pham and Nam T. Pha have contributed equally

References

[1] M. Armand, J.-M. Tarascon, Building better batteries, *Nature* **451** (2008) 652-657. http://dx.doi.org/10.1038/451652a

[2] J.-M. Tarascon, M. Armand, Issues and challenges facing rechargeable lithium batteries, *Nature* **414** (2001) 359-367. https://doi.org/10.1038/35104644

[3] V. Etacheri, R. Marom, R. Elazari, G. Salitra, D. Aurbach, Challenges in the development of advanced Li-ion batteries: a review, *Energy & Environmental Science* **4(9)** (2011) 3243-3262. https://doi.org/10.1039/C1EE01598B

[4] A. Borenstein, O. Hanna, R. Attias, S. Luski, T. Brousse, D. Aurbach, Carbon-based composite materials for supercapacitor electrodes: a review, *Journal of Materials Chemistry A* **5(25)** (2017) 12653-12672. https://doi.org/10.1039/C7TA00863E

[5] C. C. Raj, R. Prasanth, Advent of TiO_2 Nanotubes as Supercapacitor Electrode, *Journal of The Electrochemical Society* **165(9)** (2018) E345-E358. https://doi.org/10.1149/2.0561809jes

[6] G. Z. Chen, Supercapacitor and supercapattery as emerging electrochemical energy stores. *International Materials Reviews* **62(4)** (2017) 173-202. https://doi.org/10.1080/09506608.2016.1240914

[7] T. M. David, T. Mathews, Recent Advances in Hybrid Supercapacitors, *In Metal, Metal-Oxides and Metal Sulfides for Batteries, Fuel Cells, Solar Cells, Photocatalysis and Health Sensors* **62** (2021) 75-113. https://doi.org/10.1007/978-3-030-63791-0_3

[8] P. Lamba, P. Singh, P. Singh, P. Singh, Bharti; A. Kumar, M. Gupta, Y. Kumar, Recent advancements in supercapacitors based on different electrode materials: Classifications, synthesis methods and comparative performance, *Journal of Energy Storage* **48** (2022) 103871. https://doi.org/10.1016/j.est.2021.103871

[9] X. Lu, G. Wang, T. Zhai, M. Yu, J. Gan, Y. Tong, Y. Li, Hydrogenated TiO2 Nanotube Arrays for Supercapacitors, *Nano Letters* **12(3)** (2012) 1690-1696. https://doi.org/10.1021/nl300173j

[10] Poonam, K. Sharma, A. Arora, S. K. Tripathi, Review of supercapacitors: Materials and devices, *Journal of Energy Storage* **21** (2019) 801-825. https://doi.org/10.1016/j.est.2019.01.010

[11] F. Shi, L. Li, X. L. Wang, C. D. Gu, J. P. Tu, Metal oxide-hydroxide based materials for supercapacitor, *RSC Advances* **4 (79)** (2014) 41910-41921. https://doi.org/10.1039/C4RA06136E

[12] F. Naeem, S. Naeem, Y. Zhao, D. Wang, J. Zhang, Y. Mei, G. Huang, TiO2 Nanomembranes Fabricated by Atomic Layer Deposition for Supercapacitor Electrode with Enhanced Capacitance, *Nanoscale Research Letters* **14(1)** (2019) 92. https://doi.org/10.1186/s11671-019-2912-3

[13] Q. Wang, Z. H. Wen, J. H. Li, A Hybrid Supercapacitor Fabricated with a Carbon Nanotube Cathode and a TiO2–B Nanowire Anode, *Advanced Functional Materials* **16(16)** (2006) 2141-2146. https://doi.org/10.1002/adfm.200500937

[14] I. Heng, F. W. Low, C. W. Lai, J. C. Juan, N. Amin, S. K. Tiong, High performance supercapattery with rGO/TiO2 nanocomposites anode and activated carbon cathode, *Journal of Alloys and Compounds* **796** (2019) 13-24. https://doi.org/10.1016/j.jallcom.2019.04.347

[15] S. M. Benoy, M. Pandey, D. Bhattacharjya, B. K. Saikia, Recent trends in supercapacitor-battery hybrid energy storage devices based on carbon materials, *Journal of Energy Storage* **52** (2022) 104938. https://doi.org/10.1016/j.est.2022.104938

[16] S. Saini, P. Chand, A. Joshi, Biomass derived carbon for supercapacitor applications: Review, *Journal of Energy Storage* **39** (2021) 102646. https://doi.org/10.1016/j.est.2021.102646

[17] L. T. N. Huynh, T. N. Pham, T. H. Nguyen, V. H. Le, T. T. Nguyen, T. D. K. Nguyen, T. N. Tran, P. A. V. Ho, T. T. Co, T. T. T. Nguyen, T. K. A. Vo, T. H. Nguyen, T. T. Vu, V. M. Luong, H. Uyama, G. V. Pham, T. Hoang, D. L. Tran, Coconut shell-derived activated carbon and carbon nanotubes composite: a promising candidate for capacitive deionization electrode, *Synthetic Metals* **265** (2020) 116415. https://doi.org/10.1016/j.synthmet.2020.116415

[18] F. Barzegar, A. A. Khaleed, F. U. Ugbo, K. O. Oyeniran, D. Y. Momodu, A. Bello, J. K. Dangbegnon, N. Manyala, Cycling and floating performance of symmetric supercapacitor derived from coconut shell biomass, *AIP Advances* **6(11)** (2016) 115306. https://doi.org/10.1063/1.4967348

[19] J. Mi, X. R. Wang, R. J. Fan, W. H. Qu, W. C. Li, Coconut-Shell-Based Porous Carbons with a Tunable Micro/Mesopore Ratio for High-Performance Supercapacitors, *Energy & Fuels* **26(8)** (2012) 5321-5329. https://doi.org/10.1021/ef3009234

[20] G. Kresse, J. Furthmüller, Efficiency of ab-initio total energy calculations for metals and semiconductors using a plane-wave basis set, *Computational Materials Science* **6(1)** (1996) 15-50. https://doi.org/10.1016/0927-0256(96)00008-0

[21] G. Kresse, J. Furthmüller, Efficient iterative schemes for ab initio total-energy calculations using a plane-wave basis set, *Physical Review B* **54(16)** (1996) 11169. https://doi.org/10.1103/PhysRevB.54.11169

[22] P. E. Blöchl, Projector augmented-wave method, *Physical Review B* **50** (1994) 17953. https://doi.org/10.1103/PhysRevB.50.17953

[23] G. Kresse, D. Joubert, From ultrasoft pseudopotentials to the projector augmented-wave method, *Physical review B* **59(3)** (1999) 1758. https://doi.org/10.1103/PhysRevB.59.1758

[24] J. P. Perdew, K. Burke, M. Ernzerhof, Generalized gradient approximation made simple, *Physical Review Letters* **77(18)** (1996) 3865. https://doi.org/10.1103/PhysRevLett.77.3865

[25] J. P. Perdew, J. A. Chevary, S. H. Vosko, K. A. Jackson, M. R. Pederson, D. J. Singh, C. Fiolhais, Atoms, molecules, solids, and surfaces: Applications of the generalized gradient approximation for exchange and correlation, *Physical Review B* **46(11)** (1992) 6671. https://doi.org/10.1103/PhysRevB.46.6671

[26] B. Hammer, L. B. Hansen, J. K. Nørskov, Improved adsorption energetics within density-functional theory using revised Perdew-Burke-Ernzerhof functionals, *Physical Review B* **59(11)** (1999) 7413. https://doi.org/10.1103/PhysRevB.59.7413

[27] M. Ernzerhof, G. E. Scuseria, Assessment of the Perdew–Burke–Ernzerhof exchange-correlation functional, *The Journal of Chemical Physics* **110(11)** (1999) 5029-5036. https://doi.org/10.1063/1.478401

[28] N. N. Pham, K. H. Kim, B. Han, S. G. Lee, Theoretical Investigation of the Active Sites in N-Doped Graphene Bilayer for the Oxygen Reduction Reaction in Alkaline Media in PEMFCs, *The Journal of Physical Chemistry C* **126(11)** (2022) 5863-5872. https://doi.org/10.1021/acs.jpcc.1c09657

[29] N. N. Pham, S. G. Kang, Y. A. Son, S. Y. Lee, H. J. Kim, S. G. Lee, Electrochemical Oxygen-Reduction Activity and Carbon Monoxide Tolerance of Iron Phthalocyanine Functionalized with Graphene Quantum Dots: A Density Functional Theory Approach, *The Journal of Physical Chemistry C* **123(45)** (2019) 27483-27491. https://doi.org/10.1021/acs.jpcc.9b06750

[30] T. V. Tam, S. G. Kang, M. H. Kim, S. G. Lee, S. H. Hur, J. S. Chung, W. M. Choi, Novel graphene hydrogel/B-doped graphene quantum dots composites as trifunctional electrocatalysts for Zn− air batteries and overall water splitting, *Advanced Energy Materials* **9(26)** (2019) 1900945. https://doi.org/10.1002/aenm.201900945

[31] J. H. Lee, S. H. Kwon, S. Kwon, M. Cho, K. H. Kim, T. H. Han, S. G. Lee, Tunable electronic properties of nitrogen and sulfur doped graphene: Density functional theory approach, *Nanomaterials* **9(2)** (2019) 268. https://doi.org/10.3390/nano9020268

[32] N. N. Pham, J. S. Park, H. T. Kim, H. J. Kim, Y. A. Son, S. G. Kang, S. G. Lee, Catalytic performance of graphene quantum dot supported manganese phthalocyanine for efficient oxygen reduction: density functional theory approach, *New Journal of Chemistry* **43(1)** (2019) 348-355. https://doi.org/10.1039/C8NJ05093G

[33] H. J. Kwon, Y. Kwon, T. Kim, Y. Jung, S. Lee, M. Cho, S. Kwon, Enhanced competitive adsorption of CO_2 and H_2 on graphyne: A density functional theory study, *AIP Advances* **7(12)** (2017) 125013. https://doi.org/10.1063/1.5006839

[34] H. W. Lee, H. S. Moon, J. Hur, I. T. Kim, M. S. Park, J. M. Yun, K. H. Kim, S. G. Lee, Mechanism of sodium adsorption on N-doped graphene nanoribbons for sodium ion battery applications: A density functional theory approach, *Carbon* **119** (2017) 492-501. https://doi.org/10.1016/j.carbon.2017.04.033

[35] N. N. Pham, Nitrogen doping effects on the physical and chemical properties of bilayer graphdiyne: A density functional theory approach, *Applied Surface Science Advances* **11** (2022) 100301. https://doi.org/10.1016/j.apsadv.2022.100301

[36] O. L. Li, N. N. Pham, J. Kim, H. Choi, D. H. Lee, Y. Yang, W. Yao, Y. R. Cho, S. G. Lee, Insights on boosting oxygen evolution reaction performance via boron incorporation into nitrogen-doped carbon electrocatalysts, *Applied Surface Science* **528** (2020) 146979. https://doi.org/10.1016/j.apsusc.2020.146979

[37] N. N. Pham, H. Guo, S. G. Lee, Influence of phosphorus-doped bilayer graphene configuration on the oxygen reduction reaction in acidic solution, *Carbon* **220** (2023) 118012. https://doi.org/10.1016/j.carbon.2023.118012

[38] S. Grimme, J. Antony, S. Ehrlich, H. Krieg, A consistent and accurate ab initio parametrization of density functional dispersion correction (DFT-D) for the 94 elements H-Pu, *The Journal of Chemical Physics* **132(15)** (2010) 154104. https://doi.org/10.1063/1.3382344

[39] H. J. Monkhorst, J. D. Pack, Special points for Brillouin-zone integrations, *Physical Review B* **13(12)** (1976) 5188. https://doi.org/10.1103/PhysRevB.13.5188

[40] S. L. Dudarev, G. A. Botton, S. Y. Savrasov, C. Humphreys, A. P. Sutton, Electron-energy-loss spectra and the structural stability of nickel oxide: An LSDA+U study, *Physical Review B* **57(3)** (1998) 1505. https://doi.org/10.1103/PhysRevB.57.1505

[41] R. Long, N. J. English, O. V. Prezhdo, Photo-induced charge separation across the graphene–TiO2 interface is faster than energy losses: a time-domain ab initio analysis, *Journal of the American Chemical Society* **134(34)** (2012) 14238-14248. https://doi.org/10.1021/ja3063953

[42] A. Du, Y. H. Ng, N. J. Bell, Z. Zhu, R. Amal, S. C. Smith, Hybrid graphene/titania nanocomposite: interface charge transfer, hole doping, and sensitization for visible light

response, *The Journal of Physical Chemistry Letters* **2(8)** (2011) 894-899. https://doi.org/10.1021/jz2002698

[43] S. Grimme, Semiempirical GGA-type density functional constructed with a long-range dispersion correction, *Journal of Computational Chemistry* **27(15)** (2006) 1787-1799. https://doi.org/10.1002/jcc.20495

[44] H. Jónsson, G. Mills, K. W. Jacobsen, Nudged elastic band method for finding minimum energy paths of transitions. In Classical and quantum dynamics in condensed phase simulations, *World Scientific* (1998) 385-404. https://doi.org/10.1142/9789812839664_0016

[45] J. Xu, C. Jia, B. Cao, W. F. Zhang, Electrochemical properties of anatase TiO2 nanotubes as an anode material for lithium-ion batteries, *Electrochimica Acta* **52(28)** (2007) 8044-8047. https://doi.org/10.1016/j.electacta.2007.06.077

[46] L. F. Que, F. D. Yu, Z. B. Wang, D. M. Gu, Pseudocapacitance of TiO_{2-x}/CNT Anodes for High-Performance Quasi-Solid-State Li-Ion and Na-Ion Capacitors, *Small* **14(17)** (2018) 1704508. https://doi.org/10.1002/smll.201704508

[47] A. Moya, A. Cherevan, S. Marchesan, P. Gebhardt, M. Prato, D. Eder, J. J. Vilatela, Oxygen vacancies and interfaces enhancing photocatalytic hydrogen production in mesoporous CNT/TiO2 hybrids, *Applied Catalysis B: Environmental* **179** (2015) 574-582. https://doi.org/10.1016/j.apcatb.2015.05.052

[48] T. Ohsaka, F. Izumi, Y. Fujiki, Raman spectrum of anatase, TiO_2, *Journal of Raman Spectroscopy* **7(6)** (1978) 321-324. https://doi.org/10.1002/jrs.1250070606

[49] A. V. Abega, H. M. Ngomo, I. Nongwe, H. E. Mukaya, P. M. A. Kouoh Sone, X. Yangkou Mbianda, Easy and convenient synthesis of CNT/TiO_2 nanohybrid by in-surface oxidation of Ti^{3+} ions and application in the photocatalytic degradation of organic contaminants in water, *Synthetic Metals* **251** (2019) 1-14. https://doi.org/10.1016/j.synthmet.2019.03.012

[50] L. T. N. Huynh, H. H. A. Nguyen, T. T. D. Tran, T. T. T. Nguyen, T. M. A. Nguyen, T. H. La, V. M. Tran, M. L. P. Le, Electrode Composite $LiFePO_4$@Carbon: Structure and Electrochemical Performances, *Journal of Nanomaterials* **2019** (2019) 464920 https://doi.org/10.1155/2019/2464920

[51] V. H. Pham, T. D. Nguyen-Phan, X. Tong, B. Rajagopalan, J. S. Chung, J. H. Dickerson, Hydrogenated TiO2@reduced graphene oxide sandwich-like nanosheets for high voltage supercapacitor applications, *Carbon* **126** (2018) 135-144. https://doi.org/10.1016/j.carbon.2017.10.026

[52] A. Elmouwahidi, E. Bailón-García, J. Castelo-Quibén, A. F. Pérez-Cadenas, F. J. Maldonado-Hódar, F. Carrasco-Marín, Carbon–TiO2 composites as high-performance supercapacitor electrodes: synergistic effect between carbon and metal oxide phases, *Journal of Materials Chemistry A* **6(2)** (2018) 633-644. https://doi.org/10.1039/C7TA08023A

[53] J. H. Kim, H. J. Choi, H. K. Kim, S. H. Lee, Y. H. Lee, A hybrid supercapacitor fabricated with an activated carbon as cathode and an urchin-like TiO_2 as anode, *International Journal of Hydrogen Energy* **41(31)** (2016) 13549-13556. https://doi.org/10.1016/j.ijhydene.2016.06.018

[54] S. Yang, Y. Li, J. Sun, B. Cao, Laser induced oxygen-deficient TiO2/graphene hybrid for high-performance supercapacitor, *Journal of Power Sources* **431** (2019) 220-225. https://doi.org/10.1016/j.jpowsour.2019.05.016

[55] S. Dargouthi, C. Minot, B. Tangour, Structural study of TiO2 nanotube based to the (101) anatase surface, *Superlattices and Microstructures* **102** (2017) 307-313. https://doi.org/10.1016/j.spmi.2016.12.058

[56] G. Ramos-Sanchez, G. Chen, A. Harutyunyan, P. Balbuena, Theoretical and experimental investigations of the Li storage capacity in single-walled carbon nanotube bundles, *RSC Advances* **6(33)** (2016) 27260-27266. https://doi.org/10.1039/C5RA27225D

[57] G. Qi, T. Rabczuk, Ab-initio investigation of lithium adsorption on short carbon nanotubes considering effects of the tube length, *Carbon* **155** (2019) 727-733. https://doi.org/10.1016/j.carbon.2019.08.027